Investigation of ionization-induced electron injection in a wakefield driven by laser inside a gas cell

T. L. Audet,[1, a)] M. Hansson,[2] P. Lee,[1] F.G. Desforges,[1] G. Maynard,[1] S. Dobosz Dufrénoy,[3] R. Lehe,[4] J. -L. Vay,[4] B. Aurand,[2] A. Persson,[2] I. Gallardo González,[2] A. Maitrallain,[3] P. Monot,[3] C.-G. Wahlström,[2] O. Lundh,[2] and B. Cros[1, b)]

[1)] *Laboratoire de Physique des Gaz et des Plasmas, CNRS, Univ. Paris-Sud, Université Paris-Saclay, 91405, Orsay, France.*

[2)] *Department of Physics, Lund University, P.O. Box 118, S-22100 Lund, Sweden.*

[3)] *Laboratoire Interactions, Dynamique et Lasers, CEA, Université Paris-Saclay, 91191 Gif-Sur-Yvette, France.*

[4)] *Lawrence Berkeley National Laboratory, Berkeley, California 94720, USA.*

Ionization-induced electron injection was investigated experimentally by focusing a driving laser pulse with a maximum normalized potential of 1.2 at different positions along the plasma density profile inside a gas cell, filled with a gas mixture composed of $99\%H_2 + 1\%N_2$. Changing the laser focus position relative to the gas cell entrance controls the accelerated electron bunch properties, such as the spectrum width, maximum energy, and accelerated charge. Simulations performed using the 3D particle-in-cell (PIC) code WARP with a realistic density profile give results that are in good agreement with the experimental ones. The interest of this regime for optimizing the bunch charge in a selected energy window is discussed.

I. INTRODUCTION

The mechanism of laser wakefield acceleration (LWFA) in a plasma[1] can produce electric fields 3 orders of magnitude higher than in conventional RF accelerators. LWFA thus appears as a promising way to achieve compact relativistic electron sources. In this scheme the plasma wave is excited by the ponderomotive force of a short intense laser pulse. At sufficiently high intensity gradient (typically achievable with an ultrashort laser pulse with intensity above $\sim 10^{19}$ W/cm^2), plasma electrons are blown out of the laser axis behind the laser pulse. A cavity or "bubble" where only ions remain is created behind the laser pulse leading to strong transverse and longitudinal electrostatic fields. Plasma electrons can be trapped in this field and accelerated to high energy. This mechanism can occur continuously or several times over the plasma length as long as the laser intensity is high enough, which leads to accelerated electron bunches with a wide energy spread.

Several methods to increase the number of electrons and reduce the electron bunch energy spread have been proposed and tested such as the use of colliding pulses[2,3], density ramp injection[4,5], density transition injection[6,7], or ionization-induced injection[8–10]. The mechanism of ionization-induced injection can be implemented simply by adding a small proportion of high-Z gas to the low-Z gas constituting the target medium. During the interaction with the intense laser pulse, the outer shell electrons of the high-Z gas are ionized in the front of the laser pulse, and mostly contribute to the plasma wave, without being trapped. Electrons from the inner-shell of the high-Z atoms, having a much higher ionization threshold, are ionized closer to the intensity peak in a region where they can be more easily trapped by the plasma wave. This mechanism has shown its ability to increase the trapped charge[11] and lower the transverse emittance of the electron bunches[12], and is thus a promising candidate as an injector for multi-stage laser plasma accelerators. Although previous studies have used it in injector-accelerator experiments[13,14], a detailed specific study of the injection mechanism and the physics controlling the electron bunch properties in the experiments needed to be performed.

In this paper, the properties of electron bunches with energy in the range $50 - 200$ MeV, produced by ionization-induced injection using a single laser pulse focused in a gas cell target are reported. The laser normalized vector potential and maximum plasma density are such that electron injection is dominated by ionization-induced injection, as shown in previous work[11]. The focal spot position was varied along the propagation axis to explore different injection conditions along the plasma density profile.

The use of gas cells has been shown to contribute to the stability of electron production[15–18] as the gas confined in the cell is relatively homogeneous. Nevertheless, windows cannot be used to confine the gas on the intense short-pulse laser path, and density gradients are established due to gas leakage between the higher pressure volume of the gas cell and the low pressure chamber around it. Direct experimental measurement of these gradients is particularly difficult due to the small volume and large

[a)] Electronic mail: thomas.audet@u-psud.fr
[b)] Electronic mail: brigitte.cros@u-psud.fr

range of density to be probed. We have thus evaluated the gradients by their calculation through fluid simulations.

We performed experimental measurements of electron properties inside short gas cells, for which the focal plane position of the laser pulse was varied along the gradient. Experimental results were analyzed and compared with numerical modeling with the Particle-In-Cell (PIC) code WARP[19]. It shows that the density profile and the focus position play a major role in the regime of intensity studied. The remaining of the paper is organized as follows: in section II, the experimental set-up and parameters are described; section III presents experimental results of the cell position scan and their analysis with the help of simulations; the influence of other parameters such as the cell length and laser energy on the bunch properties is discussed in section IV.

II. EXPERIMENTAL CONDITIONS

Experiments were performed at the Lund Laser Centre (LLC), using a Ti:Sapphire multi-TW laser system. Linearly polarized laser pulses, with duration $\tau_L = (37 \pm 3)$ fs full-width-at-half-maximum (fwhm), were focused using a 78 cm focal length off-axis parabola to a fwhm spot size of 17 µm. The laser wavefront was corrected using a deformable mirror to achieve a symmetrical circular distribution of energy in the transverse focal plane in vacuum. The laser envelope was close to the envelope of a Gaussian pulse and the measured Rayleigh length was $z_R \simeq 1$ mm. The laser energy on target was $E_L = (585 \pm 65)$ mJ and the resulting peak intensity in the focal plane was $I_L = (3.1 \pm 0.5) \times 10^{18}$ W/cm^2, which corresponds to a normalized vector potential of $a_0 = \left(e/m_e c^2\right) \times \left(2I_L/\varepsilon_0 \omega_L\right)^{1/2} = 1.2 \pm 0.1$.

The target gas was contained in a variable length gas cell placed in the experimental vacuum chamber. The cell was made as a large diameter cylinder with replaceable entrance and exit faces, at the center of which 200 µm diameter holes were drilled to let the laser and electron bunches pass through. The thickness of the entrance and exit plates was 500 µm. A gas mixture composed of $99\%H_2 + 1\%N_2$, was let in through an electrovalve opened 40 ms before the laser pulse. The stationary state plateau gas density in the cell was characterized prior to the experiment using interferometric measurements similar to the ones described in reference[20]. Calculation of the profile with fluid simulations were performed using a transient turbulent sonic solver in OpenFOAM (sonicFoam)[21]. The normalized density profile n_e/n_{e0} obtained from simulations is plotted as a function of the position along the laser propagation axis as a solid line in Fig. 1.

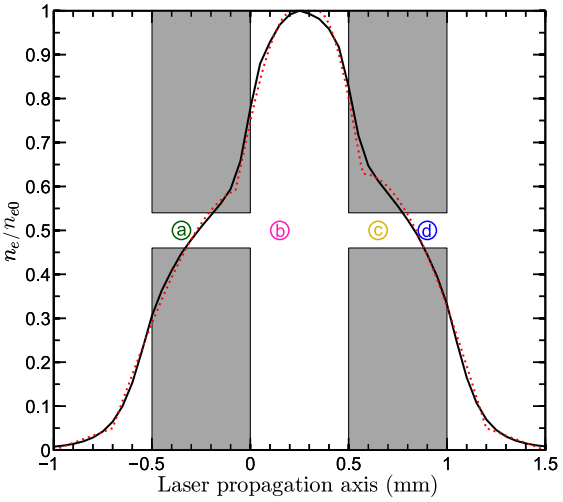

Fig. 1. Normalized density profile for an inner cell length of $L_{cell} = 0.5$ mm calculated with OpenFOAM (black solid line) and approximated density profile used in WARP simulations (red dotted line). The grey areas represent the entrance and exit plates. The colored circles are the in-vacuum focal plane positions of the laser pulse in the experimental study used for the numerical study.

The grey areas represent schematically the areas occupied by the walls of the gas cell ; the laser is propagating from left to right. The density profile consists of a maximum in the inner part of the cell which length can be varied by moving the exit plate; on each side, sharp gradients at the transition with the plates are followed by smoother gradients in the vicinity of the holes, and sharp gradients outside the cell. The colored circles, labeled (a) to (d), represent the different positions of the focal plane in-vacuum relative to the gas cell, used to achieve results shown in section III.

The focal plane is at a maximum distance of 1.4 mm from the 200 µm entry hole (in the case where it is located at 0.9 mm). In vacuum, the fwhm laser spot size at 1.4 mm from the focal plane is ~ 41 µm ; in this case, all the detected laser energy is entering the gas cell. At the LLC facility, the laser pointing is actively stabilized to cancel drift of the laser spot in the focal plane, ensuring alignment of the gas cell to be optimized and stable over time of measurement duration. For the experimental results presented in this paper, the maximum electron number density in the cell was $n_{e0} = 8.3 \times 10^{18}$ cm^{-3}, the corresponding plasma frequency is $\omega_p = 1.6 \times 10^{14}$ rad/s which leads to $\omega_p \tau_L \simeq 6$. The critical power for self-focusing associated to this density is $P_C = 3.6$ TW, which gives a ratio of laser power to critical power $P_L/P_C = (P_L[GW]/17) \times (n_e/n_c) \simeq 4.1$ where n_c is the critical density. Self-focusing is thus expected to occur mainly in the area where the density is close to its maximum.

The generated electron bunches were character-

ized using a 12 cm-long magnetic dipole with a maximum field strength of 0.7 T and a LANEX screen imaged by a 16 bits CCD. The charge was calculated from LANEX images using published calibration factor[22] and the lowest energy that could be measured was $\sim$ 50 MeV.

III. VARYING THE FOCAL PLANE POSITION

In this section, electron properties are presented for different positions of the focal plane relative to the entrance of the gas cell. Experimentally, the inner length of the cell was below 1 mm but was not known precisely. As the electron energy distribution is sensitive to the plasma length, measured electron spectra were compared to results of simulations performed for several values of the plasma length. The best fit of experimental spectra was achieved for a cell length value of $L_{cell} = 0.5$ mm.

Experimental results at different focus positions were then analyzed by comparison to quasi-three-dimensional, electromagnetic PIC simulations with the numerical code WARP, which uses a Fourier decomposition of the electromagnetic fields in the azimuthal direction with respect to the laser-propagation direction[23]. Two Fourier modes were included in the simulations. A field ionization module based on ADK model was used to model ionization dynamics[24]. The longitudinal profile calculated with OpenFOAM was used in the WARP simulations, with a maximum electron density of $n_{e0} = 7.8 \times 10^{18}$ cm^{-3}, for a gas mixture of 99% of H_2 and 1% of N_2. The laser was linearly polarized. The driving laser parameters are $a_0 = 1.1$, a spot size of 17 µm fwhm and a duration of 40 fs. All simulations were carried out with 36 macroparticles per cell with a grid resolution of $1.25 \times \lambda_L/2\pi$ and $0.05 \times \lambda_L/2\pi$ in r- and z-directions respectively.

In Fig.2(a-d) are displayed electron spectra, obtained from experimental data and from PIC simulation results, for different positions of the in-vaccuum focal plane z_f corresponding to the circles labeled (a) to (d) in Fig.1. Only electrons with energy above $\sim$ 50 MeV could be detected experimentally and grey areas around the experimental spectra represent the uncertainty on the energy determination estimated from typical electron pointing fluctuations and divergence. We can observe for all focus positions a good agreement between experimental and simulation data. The electron spectrum shape is shown to be strongly dependent on the parameter z_f. At $z_f = -0.35$ mm the spectra exhibit a plateau up to $\sim$110 MeV and then a quasi-linear decrease up to $\sim$ 150 MeV. As the value of z_f is increased, the extension of the plateau is reduced, and it vanishes at $z_f = 0.9$ mm.

Fig.3 shows experimental and simulation results for (a) the total charge above 50 MeV, Q_{tot} and (b) the maximum energy, E_{max} of the electron bunch; crosses indicate experimental points for gas mixture and open circles with lines simulation results; E_{max} is defined as the energy above which the charge density becomes less than 10% of the maximum. The value of the charge obtained by simulations was normalized to the average of the experimental values at $z_f \simeq -0.35$ mm. Triangles in Fig.3(a) are experimental results for pure H_2 for similar n_e (8.5×10^{18} cm^{-3}) and L_{cell} (0.8 ± 0.5 mm respectively). These data show that the addition of 1% N_2 increases the accelerated charge by up to a factor 10 for the range of parameters studied here, so that the injection of most electrons can be attributed to ionization-induced injection.

Simulation results and experimental data for gas mixture exhibit the same behavior. Experimental data show that both E_{max} and Q_{tot} are increasing from $z_f \simeq -0.6$ mm to $z_f \simeq -0.35$ mm. $z_f = -0.6$ mm corresponds to a position of the focal plane in vacuum in front of the entrance of the cell, so that during the propagation, the laser diffracts significantly before the density is high enough for laser pulse self-focusing to occur; consequently, the maximum intensity is relatively low, leading to a low amplitude accelerating field. From $z_f \simeq -0.6$ mm to $z_f \simeq -0.35$ mm the maximum energy is increasing, from $z_f = -0.35$ mm to $z_f = 0.15$ mm it is nearly constant and it decreases for z_f larger than 0.15 mm. The reduction of the maximum energy for z_f larger than 0.15 mm indicates a reduction of the accelerating length and/or of the accelerating field.

The evolution of the normalized vector potential a_0 along the propagation axis, as given by PIC simulations is plotted in Fig.4 with the focal plane position as a parameter. The evolution of a_0 is similar for the four cases corresponding to the spectra of Fig.2. It shows that laser focusing and defocusing are in these cases dominated by the density profile. Indeed, a_0 starts to increase around the same location for all cases which corresponds to the beginning of the laser self-focusing and decreases when the density is dropping. The variation of z_f changes the maximum absolute values of a_0, which are decreasing when z_f is increased above $z_f = 0.15$ mm.

The locations where electron injection begins is indicated by vertical dashed lines in Fig.4, they are defined as the first locations at which electrons with an energy higher than 10 MeV are present. It can be seen that the beginning of injection occurs around the same value of $a_0 \simeq 1.7\pm0.1$ for all cases which is consistent with the ionization-induced trapping threshold given in[10] (in our case at the injection we have $\gamma_p \simeq 15$ and $k_p L_{RMS} \simeq 2.1$ where γ_p is the Lorentz factor of the plasma wave, k_p its wave number and L_{RMS} the longitudinal root-mean-square laser pulse length). As z_f is increased above 1.15 mm, this value of a_0 is reached after a longer propagation distance; injection then starts

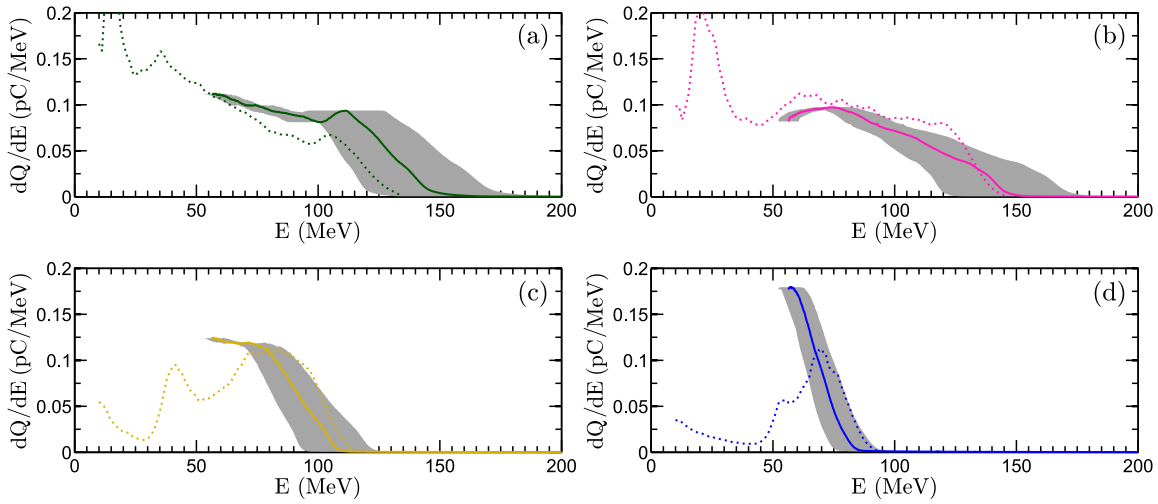

Fig. 2. Electron spectra for different positions z_f of the focal plane in vacuum, (a) : $z_f = -0.35$ mm. (b) : $z_f = 0.15$ mm. (c) : $z_f = 0.65$ mm. (d) : $z_f = 0.9$ mm. Solid lines represent the experimental spectra (averaged over 2 shots), gray areas the experimental energy uncertainty, and dotted lines represent WARP simulation results for a maximum density in the cell of $n_{e0} = 7.8 \times 10^{18}$ cm^{-3} and an inner cell length of $L_{cell} = 0.5$ mm. Simulation spectra are normalized to the maximum value of the experimental spectrum for the position $z_f = -0.35$ mm.

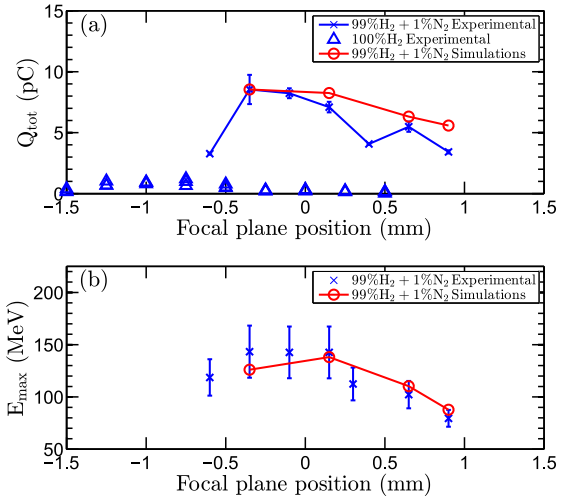

Fig. 3. Simulation and experimental results comparison for charge and energy as a function of focal plane position, blue crosses are experimental data points, red circles with solid line are simulation results : (a) Q_{tot} : bunch charge for electrons with energy higher than 50MeV ; Blue triangles represent the experimental values of the charge obtained with pure hydrogen and (b) E_{max} : electron maximal energy.

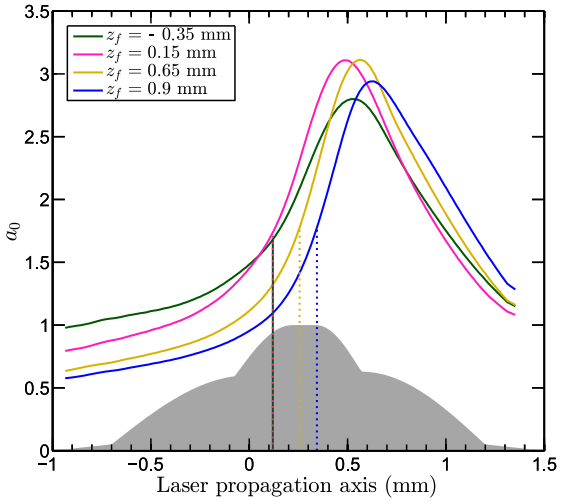

Fig. 4. Normalized vector potential obtained from WARP simulations along the propagation axis for different positions of the focal plane in vacuum. Solid lines represents the value of the normalized vector potential and vertical dashed lines indicates the start of injection in each case (for cases $z_f = -0.35$mm and $z_f = 0.15$ vertical lines are superimposed).

later and the acceleration length is reduced as the plasma length is constant.

In the simulation we also observe that the largest maximum longitudinal electric field of the wake is obtained for $z_f = 0.15$ mm. Therefore a shift of z_f away from $z_f = 0.15$ mm leads to a reduction of the length available to inject and accelerate electrons and of the amplitude of the electric field responsible for the trapping and acceleration processes. The consequence is that both the charge and the maximum energy of accelerated electrons are reduced when z_f is shifted away from $z_f = 0.15$ mm, as observed in Fig.3. These results show that a change of the laser focal plane position along the density profile allows control of the position of injection, and subsequently the accelerated charge and energy distribution.

IV. VARYING THE DENSITY, CELL LENGTH AND LASER INTENSITY

In addition to the focus position, in the regime of interest for an injector, other parameters, such as the plasma density and length, and the laser strength, have a significant role in determining the accelerated charge and the energy of the electron bunch. In this section we examine the influence of these parameters on the total charge and in a limited energy range suitable for an injector. The energy window $60-70$ MeV is of interest as it contains a significant charge for all parameter sets. Table I summarizes the parameters of 4 different cases that were studied experimentally.

Case n°	Case 1	Case 2	Case 3	Case 4
$n_e(10^{18}\,\mathrm{cm}^{-3})$	8.3	9.5	8.5	9.3
L_{cell}(mm)	0.5	0.7	10	5
$L_{cell}(L_\varphi)$	0.9	1.5	18.5	10.5
L_φ(mm)	0.56	0.46	0.54	0.48
z_f (mm)	0.9	-0.25	-0.25	-0.5

Table I. Parameters of 4 different cases for comparison of accelerated charge in experiments; n_e is the maximum value of the plateau, and the non-linear dephasing length L_φ is evaluated for this density.

The laser vector potential is $a_0 = 1.2$ and the corresponding values of the total charge, Q_{tot} (blue bars) and of the charge in the [60-70 MeV] energy range, $Q_{[60-70\mathrm{MeV}]}$ (red bars) for these 4 cases are plotted in Fig.5(a). For all cases the selected value of z_f corresponds to the focal position maximizing the charge in the 60-70 MeV energy range. Case 1 is extracted from the study presented in section III (*i.e.* $z_f = 0.9$ mm). We then compare three other sets of parameters to case 1. We first increase the density (case 2) keeping the cell length in the same range and observe a strong increase on both Q_{tot} and $Q_{[60-70\mathrm{MeV}]}$: Q_{tot} is increased by a factor ~ 12 and $Q_{[60-70\mathrm{MeV}]}$ by a factor ~ 5. Then we increase the length at a similar density (case 3), we can observe a significant increase for Q_{tot} but a decrease for $Q_{[60-70\mathrm{MeV}]}$. Finally we increase both the density and the cell length (case 4) and observe an increase for both Q_{tot} and $Q_{[60-70\mathrm{MeV}]}$.

To further understand this behavior we plotted the electron spectra for cases 1-4 in Fig.5(b). Compared to case 1 (solid black line), case 2 (solid blue line) exhibits a higher charge density over the whole spectrum and extends to higher electron energy. For case 2, as the density is higher, the laser self-focuses earlier in the profile, leading to higher charge and higher accelerating field amplitude. The length for case 3 is much longer than the dephasing length and the ionization-induced injection process is in this case continuous which explains the broad spectrum observed in Fig.5(b) (solid red line). Both the dephasing length and the

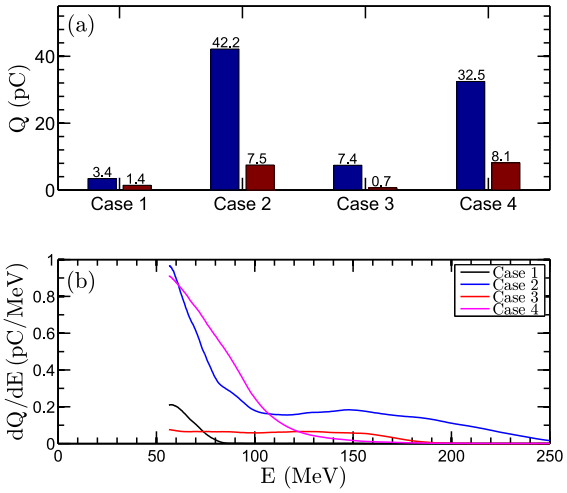

Fig. 5. Experimental cases comparison. (a) Total charge Q_{tot} (blue bars) and charge in the $60-70$ MeV energy range $Q_{[60-70\mathrm{MeV}]}$ (red bars) for parameters of Cases 1 to 4 listed in table 1; (b) Corresponding energy spectra.

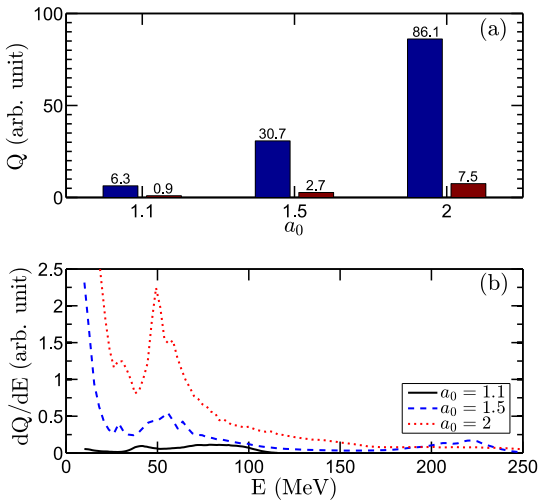

Fig. 6. (a) : Simulated electron bunches total charge Q_{tot} (blue bars) and charge in the $60-70$ MeV energy range $Q_{[60-70\mathrm{MeV}]}$ (red bars) and (b) : associated electron energy distribution for different values of a_0. Normalization is the same as in Fig.3.

depletion length at this density ($n_{e0} \sim 8.3\times10^{18}$ cm^{-3}, $L_D \simeq 2.3$ mm, $L_\varphi \simeq 0.6$ mm[25]) are larger than the cell length of case 1, therefore an increase in length compared to case 1 leads to an increase of E_{max} as seen in Fig.5(b) for case 3. For case 4 density and length are both increased, leading to an increase of accelerated charge (similar to case 2) and energy spectrum broadening (similar to case 3). In comparison with case 2 , case 4 presents a lower high energy charge density which is probably due to the dephasing effect. The comparison of these 4 cases shows that the charge in the range 60-70 MeV is maximized for larger n_{e0}, although for the set of parameters studied it reaches only 25%

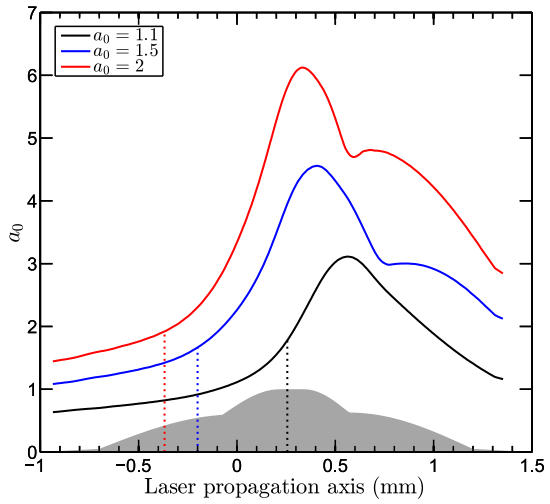

Fig. 7. Evolution of a_0 along the propagation axis for different values of a_0 in vacuum. Solid lines represents the value of the normalized vector potential and dashed lines indicates the start of injection in each case.

of the total measured charge at a value around 8 pC.

The effect of a_0 variations was studied numerically using WARP simulations, as the laser energy could not be increased in the experiment. In Fig.6, are plotted Q_{tot} and $Q_{[60-70\text{MeV}]}$ and the associated spectra at $n_{e0} = 7.8 \times 10^{18}$ cm^{-3} and $z_f = 0.65$ mm and for different values of a_0 indicated on the horizontal axis. Fig.6(a) shows that an increase of a_0 from 1.1 to 2 multiplies Q_{tot} by 13.7 and $Q_{[60-70\text{MeV}]}$ by 9.2. In Fig.6(b) we observe that the spectra exhibit higher charge density over all the spectrum for higher a_0 and a higher E_{max}. We also observe a peak appearing around 50 MeV for $a_0 = 2$ which can be of interest for an injector at this energy.

Fig.7 presents the evolutions of a_0 along the propagation axis and the beginning of injection for the different cases. For all simulation results, injection is observed when $\triangle\phi = \phi_i - \phi_{min} \simeq 1$ where ϕ_i is the normalized electrostatic potential of the plasma wave ($\phi = e\Phi/m_e c^2$) at the position of creation of electrons ionized from N^{5+} and N^{6+} and ϕ_{min} its first minimum. To satisfy this condition at a density lower than n_{e0}, *i.e.* to drive a similar amplitude plasma wave at lower density, the laser amplitude must be higher[26]. For a value in-vacuum of $a_0 = 2$ the laser power is high enough for self-focusing to occur in the entry gradient. In this case injection is observed at $n_e \simeq 0.4 \times n_{e0}$ when $a_0 \simeq 1.9$. It thus shows that increasing the initial value of a_0 and keeping z_f constant leads to injection earlier during the propagation.

For $a_0 = 1.5$ and 2 we observe significant injection of hydrogen electrons although their contribution to the spectrum is smaller than the contributions of electrons coming from ionized N^{5+} and N^{6+}. Indeed electrons from hydrogen represent ∼9% and ∼17% of the total charge in case of an initial a_0 of 1.5 and 2 respectively. We also observe that the maximum longitudinal electric field is ∼1.9 and ∼2.7 times higher for $a_0 = 1.5$ and $a_0 = 2$ respectively. Both effects, earlier injection and the excitation of larger amplitude electric fields over a longer distance contribute to produce higher charge and electron bunches with higher energy.

V. CONCLUSION

In conclusion, we showed that the position of the laser focal plane along the density profile of a gas cell plays a major role in triggering the ionization-induced injection of electrons and controlling acceleration processes, and therefore on determining the properties of generated electron bunches. Especially, we showed that the focal plane position relative to the cell entrance changes the maximum value of a_0, which has an impact on the longitudinal position of injection and electrostatic fields magnitude. By changing the focal plane position, the electron bunch charge and energy distribution can be tuned, either to optimize the electron bunch total charge or the charge in a given energy range, for example 60-70 MeV optimized to 41% of the total measured charge for the case of Fig.2(d) (case 1). For this case, the focal plane in vacuum is located in the exit density gradient ($z_f = 0.9$ mm) and $a_0 = 1.1$, simulation results show a distribution centered at ∼68 MeV. The charge in the 60-70 MeV range can be increased by a factor ∼ 5 by increasing the density (case 2). When a_0 is increased from 1.1 to 2, simulations predict 13.6 times higher charge electron bunch exhibiting a peaked distribution at ∼50 MeV.

ACKNOWLEDGMENTS

Authors acknowledge the use of the computing facility clusters GMPCS of the LUMAT federation (FR LUMAT 2764). This work was supported by the Triangle de la Physique under contract no 2012-032TELISA. Authors also acknowledge the support of the Swedish Research Council, the Knut and Alice Wallenberg Foundation, the Swedish Foundation for Strategic Research, Laserlab-Europe/CHARPAC and EuCARD2/ANAC2 (Grant Agreements No. 284464 and 312453, EC's 7th Framework Programme). This work was supported in part by the Director, Office of Science, Office of High Energy Physics, U.S. Dept. of Energy under Contract No. DE-AC02-05CH11231.

REFERENCES

[1] T. Tajima and J. M. Dawson, Phys. Rev. Lett. **43**, 267 (1979).
[2] E. H. Esarey, R. F. Hubbard, W. P. Leemans, A. Ting, and P. Sprangle, Phys. Rev. Lett. **79**, 2682 (1997).
[3] J. Faure, C. Rechatin, A. Norlin, A. F. Lifschitz, Y. Glinec, and V. Malka, Nature **444**, 737 (2006).
[4] S. V. Bulanov, N. Naumova, F. Pegoraro, and J. Sakai, Phys. Rev. E **58**, R5257 (1998).
[5] C. G. R. Geddes, K. Nakamura, G. R. Plateau, C. Tóth, E. Cormier-Michel, E. H. Esarey, C. B. Schroeder, J. R. Cary, and W. P. Leemans, Phys. Rev. Lett. **100**, 215004 (2008).
[6] K. Schmid, A. Buck, C. M. S. Sears, J. M. Mikhailova, R. Tautz, D. Herrmann, M. Geissler, F. Krausz, and L. Veisz, Phys. Rev. ST Accel. Beams **13**, 091301 (2010).
[7] M. Burza, A. Gonoskov, K. Svensson, F. Wojda, A. Persson, M. Hansson, G. Genoud, M. Marklund, C.-G. Wahlström, and O. Lundh, Phys. Rev. ST Accel. Beams **16**, 011301 (2013).
[8] M. Chen, Z.-M. Sheng, Y.-Y. Ma, and J. Zhang, J. Appl. Phys. **99**, 056109 (2006).
[9] A. Pak, K. A. Marsh, S. F. Martins, W. Lu, W. B. Mori, and C. Joshi, Phys. Rev. Lett. **104**, 025003 (2010).
[10] M. Chen, E. H. Esarey, C. B. Schroeder, C. G. R. Geddes, and W. P. Leemans, Phys. Plasmas **19**, 033101 (2012).
[11] F. G. Desforges, B. S. Paradkar, M. Hansson, J. Ju, L. Senje, T. L. Audet, A. Persson, S. D. Dufrénoy, O. Lundh, G. Maynard, P. Monot, J.-L. Vay, C.-G. Wahlström, and B. Cros, Phys. Plasmas **21**, 120703 (2014).
[12] C. McGuffey, A. G. R. Thomas, W. Schumaker, T. Matsuoka, V. Chvykov, F. J. Dollar, G. Kalintchenko, V. Y. A. Maksimchuk, K. Krushelnick, V. Y. Bychenkov, I. V. Glazyrin, and A. V. Karpeev, Phys. Rev. Lett. **104**, 025004 (2010).
[13] C. E. Clayton, J. E. Ralph, F. Albert, R. A. Fonseca, S. H. Glenzer, C. Joshi, W. Lu, K. A. Marsh, S. F. Martins, W. B. Mori, A. Pak, F. S. Tsung, B. B. Pollock, J. S. Ross, L. O. Silva, and D. H. Froula, Phys. Rev. Lett. **105**, 105003 (2010).
[14] B. B. Pollock, C. E. Clayton, J. E. Ralph, F. Albert, A. Davidson, L. Divol, C. Filip, S. H. Glenzer, K. Herpoldt, W. Lu, K. A. Marsh, J. Meinecke, W. B. Mori, A. Pak, T. C. Rensink, J. S. Ross, J. Shaw, G. R. Tynan, C. Joshi, and D. H. Froula, Phys. Rev. Lett. **107**, 045001 (2011).
[15] J. Osterhoff, A. Popp, Z. Major, B. Marx, T. P. Rowlands-Rees, M. Fuchs, M. Geissler, R. Hörlein, B. H. S. Becker, E. A. Peralta, U. Schramm, F. Grüner, D. Habs, F. Krausz, S. M. Hooker, and S. Karsch, Phys. Rev. Lett. **101**, 085002 (2008).
[16] M. Vargas, W. Schumaker, Z.-H. He, Z. Zhao, K. Behm, V. Chvykov, B. Hou, K. Krushelnick, A. Maksimchuk, V. Yanovsky, and A. G. R. Thomas, Appl. Phys. Lett. **104**, 174103 (2014).
[17] F. G. Desforges, M. Hansson, J. Ju, L. Senje, T. L. Audet, S. Dobosz-Dufrénoy, A. Persson, O. Lundh, C.-G. Wahlström, and B. Cros, Nucl. Instrum. Meth. A **740**, 54 (2013).
[18] M. Hansson, L. Senje, A. Persson, O. Lundh, C.-G. Wahlström, F. G. Desforges, J. Ju, T. L. Audet, B. Cros, S. D. Dufrénoy, and P. Monot, Phys. Rev. ST Accel. Beams **17**, 031303 (2014).
[19] J.-L. Vay, D. P. Grote, R. H. Cohen, and A. Friedman, Comput. Sci. Disc. **5**, 014019 (2012).
[20] J. Ju and B. Cros, J. Appl. Phys. **112**, 113102 (2012).
[21] "Openfoam documentation," (2014), `http://www.openfoam.com`.
[22] A. Buck, K. Zeil, A. Popp, K. Schmid, A. Jochmann, S. D. Kraft, B. Hidding, T. Kudyakov, C. M. S. Sears, L. Veisz, S. Karsch, J. Pawelke, R. Sauerbrey, T. Cowan, F. Krausz, and U. Schramm, Rev. Sci. Instrum. **81**, 033301 (2010).
[23] A. Lifschitz, X. Davoine, E. Lefebvre, J. Faure, C. Rechatin, and V. Malka, J. Comput. Phys. **228**, 1803 (2009).
[24] G. L. Yudin and M. Y. Ivanov, Phys. Rev. A **64**, 013409 (2001).
[25] W. Lu, M. Tzoufras, C. Joshi, F. S. Tsung, W. B. Mori, J. M. Vieira, R. A. Fonseca, and L. O. Silva, Phys. Rev. ST Accel. Beams **10**, 061301 (2007).
[26] L. M. Gorbunov and V. I. Kirsanov, Sov. Phys. JETP **66**, 290 (1987).